PAPER

Spatiotemporal control of structure and dynamics in a polar active fluid†

Saptorshi Ghosh,[a] Chaitanya Joshi, [ID][b] Aparna Baskaran [ID]*[a] and
Michael F. Hagan [ID]*[a]

We apply optimal control theory to a model of a polar active fluid (the Toner–Tu model), with the objective of driving the system into particular emergent dynamical behaviors or programming switching between states on demand. We use the effective self-propulsion speed as the control parameter (*i.e.* the means of external actuation). We identify control protocols that achieve outcomes such as relocating asters to targeted positions, forcing propagating solitary waves to reorient to a particular direction, and switching between stationary asters and propagating fronts. We analyze the solutions to identify generic principles for controlling polar active fluids. Our findings have implications for achieving spatiotemporal control of active polar systems in experiments, particularly *in vitro* cytoskeletal systems. Additionally, this research paves the way for leveraging optimal control methods to engineer the structure and dynamics of active fluids more broadly.

I. Introduction

Active systems are a diverse class of non-equilibrium assemblies composed of anisotropic components that transform stored or ambient energy into motion. Idealized realizations that have contributed to the development and refinement of this conceptual framework include bacterial suspensions,[1–3] minimal systems of purified cytoskeletal proteins,[4–11] synthetic self-propelled colloids,[12–14] swarming bacterial cells,[15–19] and model tissues and cell sheets.[20–32] In these systems, the interplay between internal activity and the interactions among the active agents results in a wide range of emergent collective behaviors.[33–38] These behaviors emerge spontaneously without requiring a central control mechanism. However, there is typically no means to select which behavior emerges or to switch between states, which significantly limits the functionality of active materials.

Recent experimental advances have put the objective of control within our reach. Experiments have demonstrated that light can be used as a control field to assemble self-limited functional structures in active colloids[39,40] and to exert spatiotemporal control of motility induced phase-separation (MIPS).[41,42] By shining sequences of light that vary in space and time on active materials constructed with light-activated motor proteins, researchers can control the average speed of active flows[43,44] and steer defects in active nematics,[45] and drive the formation and movement of asters in isotropic suspensions.[46]

Theoretical progress toward functionalizing active matter has taken two paths. The first has been to impose spatiotemporal activity patterns and observe their effects on the system dynamics,[45,47–49] thereby identifying easily accessible target states. The second is to use the framework of optimal control[50,51] and optimal transport[52] to identify spatiotemporal activity patterns that will drive the system to a pre-chosen target dynamics.[47,53,54]

The work described in this article belongs in this second class. We study the optimal control theory of the classic active matter theory, a dry 2D active polar fluid, first considered by Toner and Tu.[55,56] We treat the convective speed of the active particles as the control parameter and identify control solutions that drive the system to targeted steady states, including forcing an aster to move to a given spatial location, causing propagating stripes to reorient along a particular direction, and driving a propagating stripe to convert into a stationary aster. In the previous work most closely related to this one, Norton *et al.*[53] obtained a control solution to switch a confined active nematic between two symmetric attractors (changing handedness of a circular flow state). Here, we show that an optimal control framework can solve much more diverse problems, including switching among attractors with very different broken symmetry patterns and driving the system into states which are not stable attractors at a given set of parameters.

[a] *Martin Fisher School of Physics, Brandeis University, Waltham, Massachusetts 02453, USA. E-mail: aparna@brandeis.edu, hagan@brandeis.edu*
[b] *Department of Physics and Astronomy, Tufts University, Medford, Massachusetts 02155, USA*

Further, we analyze the identified optimal solutions to uncover generic control principles that are broadly applicable to active polar fluids.

This paper is laid out as follows. In Section II, we review the hydrodynamic theory and describe the key features of the steady states that arise in the absence of control. Section III describes the method for implementing optimal control theory. In Section IV, we report the results of the control solutions for driving the system to particular steady states or switching between them. Then, we analyze the control solutions in terms of the dynamical equations of motion to identify the essential mechanisms that drive the system into the desired behavior, with the goal of identifying generic principles. We also investigate how robust the optimal control solutions are to errors arising from experimental noise and inaccuracies in model parameters. Finally Section V concludes with a discussion on testing these results in experiments.

II. Model

We consider a macroscopic description of an active polar fluid in 2D, in terms of a conserved density field $\rho(\mathbf{r},t)$ and the polarization field $\boldsymbol{\tau}(\mathbf{r},t) = \rho(\mathbf{r},t)\mathbf{P}(\mathbf{r},t)$, a vector characterizing orientational order in the fluid. As noted by Toner and Tu,[55] the order parameter is also a velocity that convects mass in an active fluid. While a number of distinct dynamical equations for these hydrodynamic quantities have been considered in the literature,[57-60] the particular model we study is of the form

$$\partial_t \rho = -\boldsymbol{\nabla}\cdot(\omega\boldsymbol{\tau} - D\boldsymbol{\nabla}\rho) \qquad (1)$$

$$\partial_t \boldsymbol{\tau} + \lambda_1 \boldsymbol{\tau}\cdot\boldsymbol{\nabla}\boldsymbol{\tau} = -\nu(a_2(\rho) + a_4(\rho)|\boldsymbol{\tau}|^2)\boldsymbol{\tau} - \boldsymbol{\nabla}(\omega\rho) + K\boldsymbol{\nabla}^2\boldsymbol{\tau}$$
$$+ \lambda_2\boldsymbol{\tau}_\alpha\boldsymbol{\nabla}\boldsymbol{\tau}_\alpha + \lambda_3\boldsymbol{\tau}\boldsymbol{\nabla}\cdot\boldsymbol{\tau}. \qquad (2)$$

We briefly discuss the physics it captures and the emergent phenomenology that results from it. Extensive studies can be found in prior work on this model.[61-65]

The density dynamics eqn (1) is an advection-diffusion equation where the advective velocity is proportional to the orientational order parameter $\mathbf{P}(\mathbf{r},t)$. The dynamics of the orientational order has three features: (i) It has a self-convection term with coefficent λ_1, encoding the absence of Galilean invariance in the 'dry' theory.[55,56] (ii) It has terms consistent with model A dynamics that drive the system downhill on a free energy landscape where $F = \int_{\mathbf{r}} \frac{a_2(\rho)}{2}|\boldsymbol{\tau}|^2 + \frac{a_4(\rho)}{4}|\boldsymbol{\tau}|^4 + \frac{K}{2}(\partial_\alpha \tau_\beta)(\partial_\alpha \tau_\beta) + \frac{\lambda}{2}|\boldsymbol{\tau}|^2\boldsymbol{\nabla}\cdot\boldsymbol{\tau}$, encoding the fact that the flocking occurs due to spontaneous symmetry breaking. (iii) It contains a hydrostatic pressure term of the form $P \equiv \omega\rho - \frac{\lambda_2}{2}|\boldsymbol{\tau}|^2$, where λ_2 encodes the tendency for elongated self-propelled particles to splay due to recollision events.[62,66,67]

In this study of spatiotemporal control, we choose $a_2(\rho) = (1 - \rho/\rho_c)$ and $a_4(\rho) = (1 + \rho/\rho_c)/\rho^2$, yielding a continuous mean-field transition from an isotropic $\boldsymbol{\tau}$ to a homogeneous, polar or a swarming state ($|\boldsymbol{\tau}| > 0$) at the critical density $\rho = \rho_c$.

For simplicity, we choose $D = K$. Without loss of generality we set the critical density $\rho_c = 1$. We further reduce the number of independent parameters and set $\lambda_1 = \lambda_2 = \lambda_3$. We set the unit of time as $\tau_0 = \nu^{-1}$, the relaxation time scale of the orientation field, and the unit of length as $l_0 = (D/\nu)^{\frac{1}{2}}$. The simplified dimensionless equations are:

$$\partial_t\rho = -\boldsymbol{\nabla}\cdot(\omega\boldsymbol{\tau} - \boldsymbol{\nabla}\rho) \qquad (3)$$

$$\partial_t\boldsymbol{\tau} = -(a_2(\rho) + a_4(\rho)|\boldsymbol{\tau}|^2)\boldsymbol{\tau} - \boldsymbol{\nabla}(\omega\rho) + \boldsymbol{\nabla}^2\boldsymbol{\tau} + \lambda(\tau_\alpha\boldsymbol{\nabla}\tau_\alpha + \boldsymbol{\tau}\boldsymbol{\nabla}\cdot\boldsymbol{\tau} - \boldsymbol{\tau}\cdot\boldsymbol{\nabla}\boldsymbol{\tau}). \qquad (4)$$

These reduced equations involve three parameters: (1) The self-propulsion speed or activity, ω, is the main control variable and dictates both density advection and an effective pressure/compressibility; (2) λ captures the interplay between interparticle interactions and activity; and (3) the mean density, ρ_0, which is set by the initial condition. We note that if these equations are derived from a microscopic model of self-propelled particles with aligning interactions, the $\{\lambda_i\}$ parameters would be complex functions of multiple parameters from the microscopic model, including the activity strength. To simplify the analysis we have set them all equal to λ and independent of activity. The system behaviors are not qualitatively affected by neglecting this dependence.[62,66,68,69] Additional discussion of these equations and other related models can be found in ref. 62, 66 and 67 and review articles.[37,38,70]

The phenomenology of this model is described in ref. 62 and summarized in Fig. 1a. For the purposes of this work, we note that the dynamics of this system admits two inhomogeneous steady states: (i) propagating stripes composed of ordered swarms moving through a disordered background, which are referred to as polar drops elsewhere in the literature,[63,71] when $\omega/\lambda \gg 1$, and (ii) a stationary high density aster, again in an isotropic background, when $\lambda/\omega \gg 1$. Both of these states arise close to the threshold density for orientational ordering (which we set to $\rho_c = 1$), and correspond to the system phase separating into a dense ordered phase and a dilute disordered phase. In this study, we fix the homogeneous density at $\rho = 1.07$ and consider the problem of controlling the inhomogeneous steady states using spatiotemporal patterning of the convective strength ω, referred to as the activity or control parameter in the rest of this paper.

This model has the virtue of mathematical simplicity and a minimal number of parameters, thus enabling physical insight from the optimal control solutions. At the same time, the states we seek to control are directly realizable in experiments (see Section V). Further, in the ESI,† we show that this theory is linearly controllable on short length scales. Thus it is ideal for investigating applications of optimal control in active systems.

III. Optimal control

Spatiotemporal control of the system involves identifying an activity field $\omega(\mathbf{r},t)$ in an interval $t \in [0,t_F]$ such that the state of the system evolves from some initial condition $\rho(\mathbf{r},0), \boldsymbol{\tau}(\mathbf{r},0)$ to a chosen target state $\rho^\star(\mathbf{r},t), \boldsymbol{\tau}^\star(\mathbf{r},t)$ within the control window
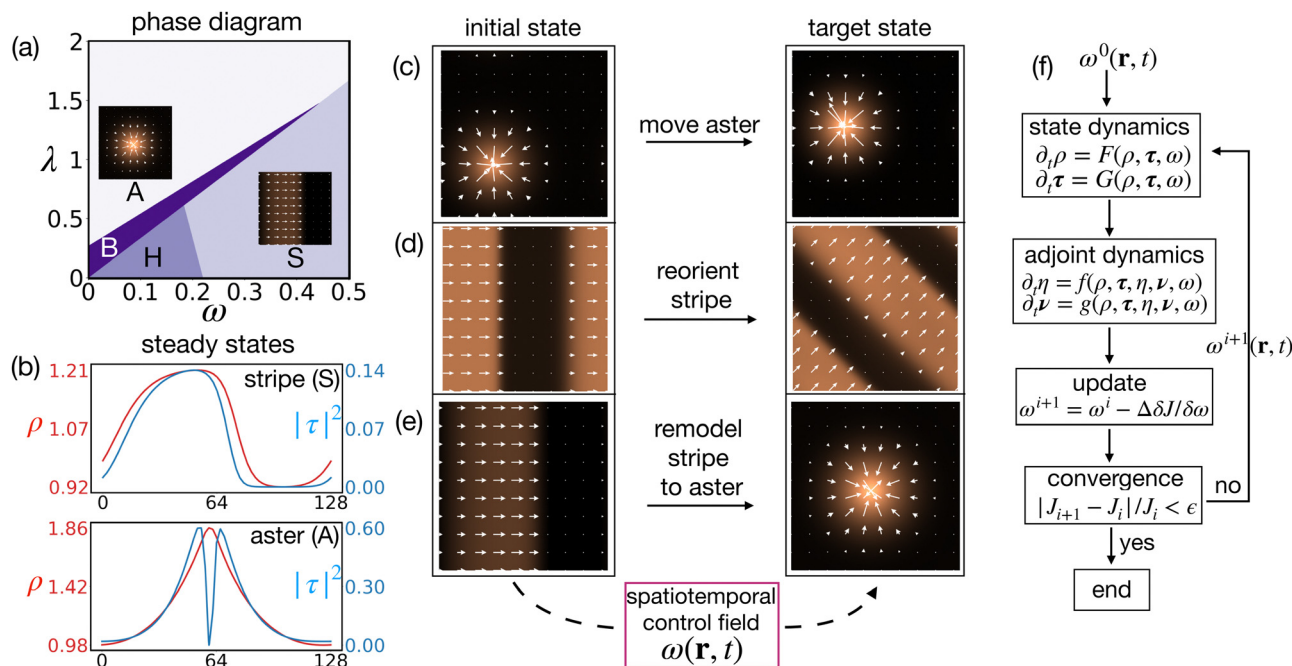
Fig. 1 Phenomenology of the bulk active polar fluid in the absence of control: (a) phase diagram and representative snapshots of the inhomeogenous steady states as a function of model parameters λ and ω, with the mean density set to $\rho_0 = 1.07$. The propagating stripes ('S') and asters ('A') are phase-separated domains of high polar order in a background of a low density disordered state. The intermediate state 'B' (which is not relevant for the present work) corresponds to a state of transient blobs of polar order coexisting with a disordered background. 'H' is the homogeneous state. (b) Linear scans of the density ρ and magnitude of polarization field τ along the direction perpendicular to the interface of the phase-separated domains. In the stripes, the polar order is homogeneous in the domain while the aster is a domain of high splay with a defect with topological charge +1 at its center. (c)–(e) Illustration of optimal control goals considered in this study. (f) Schematic of the method that we use to solve the optimal control problem, the direct adjoint looping (DAL) method.

[0,t_F]. In the optimal control framework, we identify such a solution by minimizing the scalar objective function

$$\mathcal{J} = \int_0^{t_F} dt \int_\Omega d\mathbf{r} \left[\frac{A}{2}(\bar{\omega}^2 - \bar{\omega}_0^2)^2 + \frac{B}{2}\boldsymbol{\nabla}\bar{\omega}^2 \cdot \boldsymbol{\nabla}\bar{\omega}^2 \right. \tag{5}$$
$$\left. + \frac{K}{2}(d\bar{\omega}^2/dt)^2 + \frac{C}{2}(\rho - \rho^\star)^2 + \frac{D}{2}(\boldsymbol{\tau} - \boldsymbol{\tau}^\star)^2 \right]$$

subject to the constraints that the dynamical fields $\rho(\mathbf{r},t)$, $\boldsymbol{\tau}(\mathbf{r},t)$ obey eqn (3) and (4) at every time point in the control window. We include the activity as $\omega = \bar{\omega}^2$ to constrain the solution to positive activity values, since $\omega < 0$ is unphysical in this system. The term $(\bar{\omega}^2 - \bar{\omega}_0^2)^2$ penalizes deviations of the magnitude of the control variable ω from the preferred (*i.e.* baseline) value of the activity $\omega_0 = \bar{\omega}_0^2$, and thereby restrains the control solution to the vicinity of a chosen value of activity. The terms $\frac{B}{2}\boldsymbol{\nabla}\bar{\omega}^2 \cdot \boldsymbol{\nabla}\bar{\omega}^2$ and $\frac{K}{2}(d\bar{\omega}^2/dt)^2$ promote smoothness of the activity field in space and time. To simplify the presentation of results, we set $K = 0$ and thus do not penalize time-variations.

The terms $(\rho - \rho^\star)^2$ and $(\boldsymbol{\tau} - \boldsymbol{\tau}^\star)^2$ measure the deviations from the target state, $\rho^\star$ and $\boldsymbol{\tau}^\star$. We constrain our search of optimal state trajectories to those that obey the system dynamics by introducing Lagrange multipliers, η and $\boldsymbol{\nu}$, which are adjoint variables for ρ and $\boldsymbol{\tau}$. These dynamical constraints are enforced in the optimization by adding them to the cost function as

$$\mathcal{L} = \mathcal{J} + \int_0^{t_F} dt \int_\Omega d\mathbf{r}[\eta(\partial_t\rho + \ldots) + \boldsymbol{\nu} \cdot (\partial_t\boldsymbol{\tau} + \ldots)]. \tag{6}$$

The necessary condition for optimality is $\nabla\mathcal{L} = 0$,[72,73] so $\delta\mathcal{L}/\delta\eta$, $\delta\mathcal{L}/\delta\boldsymbol{\nu}$, $\delta\mathcal{L}/\delta\rho$, $\delta\mathcal{L}/\delta\boldsymbol{\tau}$, $\delta\mathcal{L}/\delta\bar{\omega}$, $\delta\mathcal{L}/\delta\rho(t_F)$, $\delta\mathcal{L}/\delta t(t_F) = 0$. The first two conditions return eqn (3) and (4) governing ρ and $\boldsymbol{\tau}$. The following two conditions yield the dynamical equations for the adjoint variables η and $\boldsymbol{\nu}$,

$$\partial_t\eta = C(\rho - \rho^\star) - \boldsymbol{\nabla}^2\eta - \bar{\omega}^2\boldsymbol{\nabla}\cdot\boldsymbol{\nu} + (\delta_\rho a_2(\rho) + \delta_\rho a_4(\rho)|\boldsymbol{\tau}|^2)(\boldsymbol{\nu}\cdot\boldsymbol{\tau}). \tag{7}$$

$$\partial_t\boldsymbol{\nu} = D(\boldsymbol{\tau} - \boldsymbol{\tau}^\star) + (a_2(\rho) + a_4(\rho)|\boldsymbol{\tau}|^2)\boldsymbol{\nu} + 2a_4(\rho)\boldsymbol{\tau}(\boldsymbol{\nu}\cdot\boldsymbol{\tau}) - \lambda[-\boldsymbol{\tau}\boldsymbol{\nabla}\cdot\boldsymbol{\nu} + 2\boldsymbol{\nu}\boldsymbol{\nabla}\cdot\boldsymbol{\tau} - \boldsymbol{\nabla}(\boldsymbol{\nu}\cdot\boldsymbol{\tau}) + \boldsymbol{\tau}\cdot\boldsymbol{\nabla}\boldsymbol{\nu} - \nu_\alpha\boldsymbol{\nabla}\tau_\alpha] - \boldsymbol{\nabla}^2\boldsymbol{\nu} - \bar{\omega}^2\boldsymbol{\nabla}\eta. \tag{8}$$

with boundary conditions at t_F: $\{\eta,\boldsymbol{\nu}\}(\mathbf{r},t_F) = 0$, and periodic boundary conditions on the domain. $\delta\mathcal{J}/\delta\bar{\omega} = 0$ yields an equation to update the control input as,

$$2A\bar{\omega}(\bar{\omega}^2 - \bar{\omega}_0^2) - 2B\bar{\omega}\boldsymbol{\nabla}^2\bar{\omega}^2 - 2K\bar{\omega}(d^2\bar{\omega}^2/dt^2)$$
$$- 2\bar{\omega}\boldsymbol{\tau}\cdot\boldsymbol{\nabla}\eta - 2\bar{\omega}\boldsymbol{\nu}\cdot\boldsymbol{\nabla}\rho = 0. \tag{9}$$

We use the direct-adjoint-looping (DAL) method[74] to minimize the cost function under the constraint that the dynamics satisfies eqn (3) and (4), to yield the optimal schedule of activity in space and time (see ESI† Sections SIV and SV for more details).

Specifically, we construct an initial condition by performing a simulation with unperturbed dynamics (eqn (3) and (4)) until reaching steady-state, at a parameter set that leads to a desired initial behavior. We construct a target configuration in the same manner, using a different parameter set that leads to the desired target behavior. We also specify a time duration t_F over which the control protocol will be employed, and an initial trial control protocol. We then perform a series of DAL iterations; in each iteration the system and the adjoint dynamics are integrated from the initial condition for time t_F under the current control protocol, and the cost function (eqn (5)) is computed from the resulting trajectory. The adjoint equations are integrated backwards in time to propagate the residuals. After each backward run, the control protocol is updated *via* gradient descent, $\bar{\omega}^{i+1} = \bar{\omega}^i - \Delta\delta\mathcal{J}/\delta\bar{\omega}$, to minimize the cost function. We employ Armijo backtracking[75] to adaptively choose the step-size for gradient descent and to ensure convergence of the DAL algorithm. Once the optimal spatiotemporal activity pattern has been computed, performing a forward integration using eqn (3) and (4), the same initial condition, and $\omega = \bar{\omega}^2$ will yield the solution trajectory. We have implemented this entire calculation in the open-source Python finite element method solver FEniCS.[76] We have provided the associated source code and data here.

IV. Results

Using the optimal control framework described in Section III and the hydrodynamic equations eqn (3) and (4), we have computed spatiotemporal control solutions that steer the system state toward the target configuration, for each of the target behaviors shown in Fig. 1(c)–(e). In this section, we describe these calculations, and physical insights that can be learned by studying the computed control solutions.

A. Aster advection

First, starting in a parameter regime where a stationary aster is stable ($\omega = 0.05$ and $\lambda = 0.8$), we seek to advect an aster to a new location. The control problem specifies the initial and final states of the system as well as the elapsed time; that is, the spatial dependence of the density and polarization fields at every point in space at times $t = 0$ and $t = t_F = 2000$.

Fig. 2 summarizes the results of this computation. Fig. 2a and b respectively show the time evolution of the system configuration and the applied control field that drives the transformation. At early times, the applied control is strongest at the aster core while it is lowest in front of the aster along the direction we seek to move it. The aster then elongates to assume a comet-like shape, with a denser, polar-ordered head (see snapshots at $t = 50, 100$), as it advects toward the target location. Note that the activity is largest to the rear of the aster in this region. Thus, the control solution pushes (rather than pulls) the aster.

To quantify how the position and profile of the aster change over the course of advection, we measure its center-of-mass position (x_{COM}, y_{COM}) and asphericity. Here, we track the y-coordinate of the center of mass, which is calculated as $y_{COM} = \sum_{ij:\rho_{ij} > \rho_0} j\rho_{ij} \Big/ \sum_{ij:\rho_{ij} > \rho_0} \rho_{ij}$, and the asphericity is given by the ratio of eigenvalues of shape tensor: $\mathcal{I}_{\alpha\beta} = \sum_{ij:\rho_{ij} > \rho_0} \rho_{ij}\left(\|\mathbf{r}_{ij}\|^2\delta_{\alpha\beta} - r_\alpha^{ij}r_\beta^{ij}\right)$, where Latin indices denote grid points and Greek indices correspond to Cartesian coordinates, and r_{ij} is the distance of the ijth grid point from the center of mass. As shown in Fig. 2c, the control window naturally partitions into two stages. During the initial stage ($0 < t \lesssim 100$) the aster rapidly changes shape into the comet-like configuration, as seen by the decrease in its asphericity, while simultaneously undergoing advection, moving towards the target point. Then, over the remaining long time window ($100 \lesssim t < t_F$) the aster reforms slowly, the asphericity increases back to 1, and it moves the remaining small distance to the target position.

For further description of the aster profile during these stages, we present the angle of the polarization field θ as a function of the azimuthal angle ϕ around the aster core at four time points in Fig. 2d. At the initial time ($t = 0$) the system is radially symmetric with polarization vectors pointing toward the aster center, while by $t = 50$ and $t = 100$ the symmetry of θ in the top $[0,\pi]$ and bottom $[-\pi,0]$ quadrants is broken, with more polarization at the bottom points toward the advection direction, and the front-end remains aster-like with a radial configuration. The orientation returns to the aster configuration by $t = t_F$.

Further, we can understand the control solution physically by noting that the dynamics of τ is such that gradients in the control field ω create a torque on the orientation field, *i.e.*, $\partial_t\tau \sim -\rho\nabla\omega$ or equivalently $\partial_t\theta \sim \nabla\omega \times \tau$. We then calculate the integral of the torque $\left(\tau_\pm = \int_{\Omega'}\partial_t\theta\right)$ over two domains, Ω_L: $[x \in \{x_0 - 10, x_0\}, y \in \{0, L_y\}]$ on the left and and Ω_R: $[x \in \{x_0, x_0 + 10\}, y \in \{0, L_y\}]$ to the right, with $x_0 = 40$ in our case (Fig. 2e). When the aster unwinds and advects, the region to the left has a positive torque (countercockwise rotation) and the region on the right experiences negative torque (clockwise rotation), which correspond to the partial unwinding of the aster. This is also illustrated by the snapshot shown for $t = 35$, where the dashed line ($x = 40$) represents the axis along the aster's motion. During the subsequent reformation phase, as the aster regains circular symmetry, the profile winds back such that the left/right subdomains experience clockwise/counterclockwise torque respectively. The snapshot shown at $t = 1000$ illustrates this behavior. Eventually, the system relaxes sufficiently close to an unperturbed aster configuration that the net torque becomes zero.

1. Specifying the trajectory of aster advection. A limitation of the approach described thus far is that convergence of the control solution becomes unreliable when trying to advect the aster over distances significantly greater than its size ($\Delta y \approx 30$). This is because the gradients in the objective function are extremely shallow for the initial stages of the trajectory when the target state is far from the initial state. While techniques to find global minima can potentially overcome this problem,
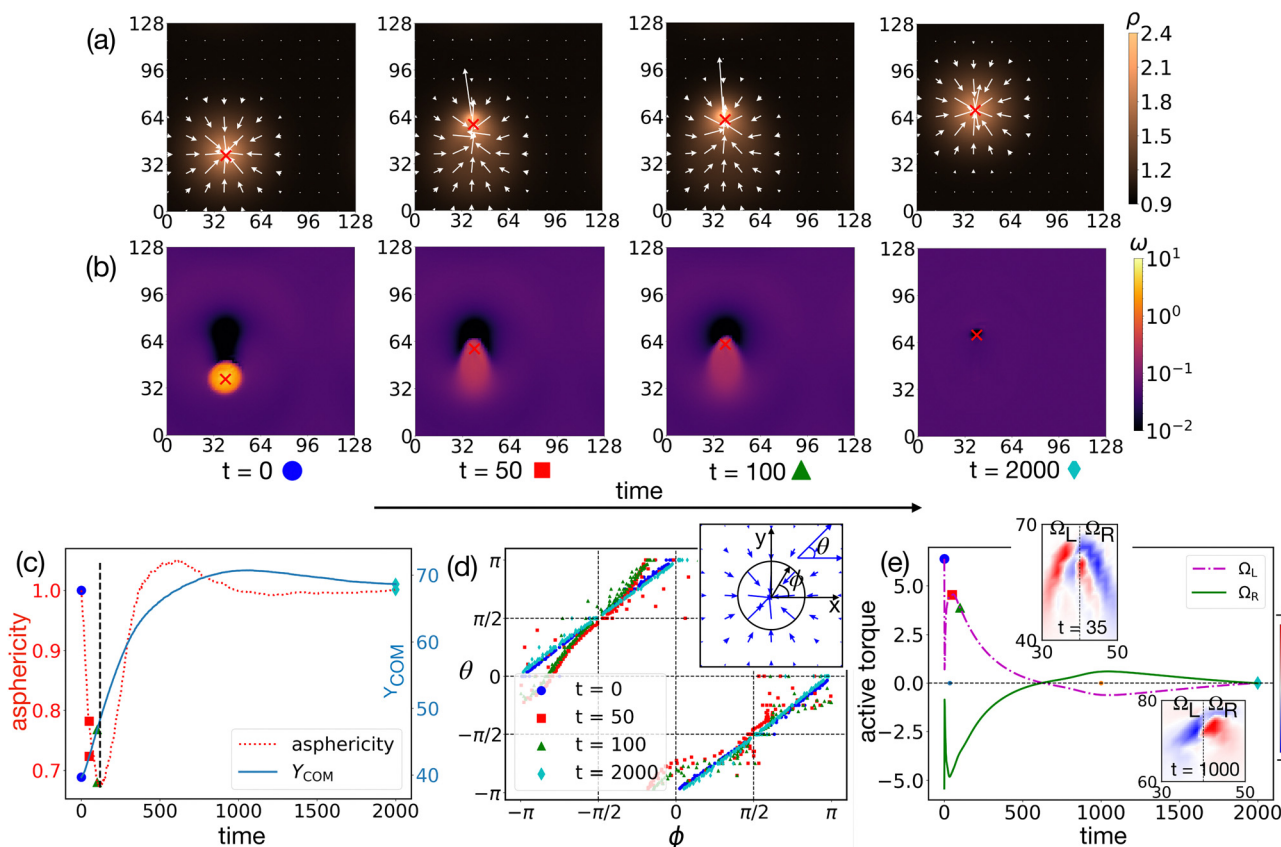
Fig. 2 Advecting an aster. The control solution for moving an aster from $(x_I = 60, y_I = 40)$ at $t = 0$ to $(x_F = 60, y_F = 70)$ at time $t_F = 2000$. All length and timescales are presented in dimensionless units, which are defined in Section II. (a) and (b) Snapshots of (a) the density ρ (color map) and polarization τ (arrows) profiles and (b) the control solution activity field ω (color map). The 'x' symbols in the snapshots in (a) and (b) show the position of the aster core. At times $t = 50, 100$ the upper quadrant of the aster unwinds and the aster becomes prolate while the aster core maintains the +1 defect. At $t = 2000$ the aster is reformed at the target location. (c) Analysis of the aster shape: the left y-axis shows the asphericity of the aster (defined as the ratio of eigenvalues of the shape tensor, see Section IV A) and the right y-axis shows the y-coordinate of the center of mass of the aster as a function of time. (d) The aster profile, as characterized by the polarization direction θ as a function of the azimuthal angle ϕ around the aster center (defined as the position at which the density is maximum, which coincides with the defect core, where $\tau = 0$). The measurement is taken at radius $r = 20$ from the core. (e) The active torque, $\nabla \omega \times \tau$, integrated over the left, Ω_L, and right, Ω_R, subdomains of the aster (see Section IV A) as a function of time, showing the driving forces for unwinding and closing of the aster in each subdomain due to activity gradients. The objective function parameters are $\{A, B, C, D, K, \omega_0\} = \{0.1, 1.0, 2.0, 2.0, 0, 0.05\}$, $\lambda = 0.8$, and the simulation box size is 128×128. A video of this trajectory is in ESI† Movie S1.

an alternative approach is to change the objective function to ensure sufficient gradients at all stages. A simple example of the latter strategy is to prescribe the entire trajectory of the aster. This approach has the added benefit of controlling the translocation speed, but has the potential drawback of arriving at a suboptimal solution (either slower translocation or higher control cost), since the problem is more constrained.

We applied the latter strategy to the problem of translocating an aster a distance of $\Delta \bar{y} = 120$. We formulated the control problem to translocate the aster at a constant speed $\bar{v}$ for a time t_{adv}, followed by a time t_{reform} for reformation of the aster. We set the target trajectory as a series of configurations in which the initial state with an aster has been translated by 1 additional unit along the translocation axis. The configurations are separated by a time increment $\Delta \bar{t} = t_{adv}/\Delta \bar{y}$, so that in the final target state configuration at time $t = t_{adv}$, the aster center-of-mass will have traveled $\Delta \bar{y}$, with a mean advection speed of $\bar{v}$. We then allow the additional time t_{reform} for the aster to acquire

its target profile. We find that specifying the path in this way allows specifying a target distance that is arbitrarily far without any difficulties in achieving convergence of the control solution.

Fig. 3a and b show the system configurations and corresponding control solution ω for an example with $\bar{v} = 1/20$, $t_{adv} = 2400$, and $t_{reform} = 1200$. At $t = 0$, the activity is maximum at the core of the aster, but unlike the previous setup where only initial and final state of the aster are specified, the order of magnitude remains same throughout the advection phase of aster. During the first phase of the solution (constant advection), the aster undergoes partial dissolution and, as intended, a roughly steady rate of translation toward the target (see snapshots at $t = 1200, 1900$). However, because we specified the trajectory at discrete intervals spaced by $\Delta \bar{y} = 1$, the optimal control field oscillates with a period of about $\Delta \bar{t} \approx \Delta \bar{y}/\bar{v} = 20$. These oscillations arise due to the discrete nature of the objective function that we have imposed, and thus they are
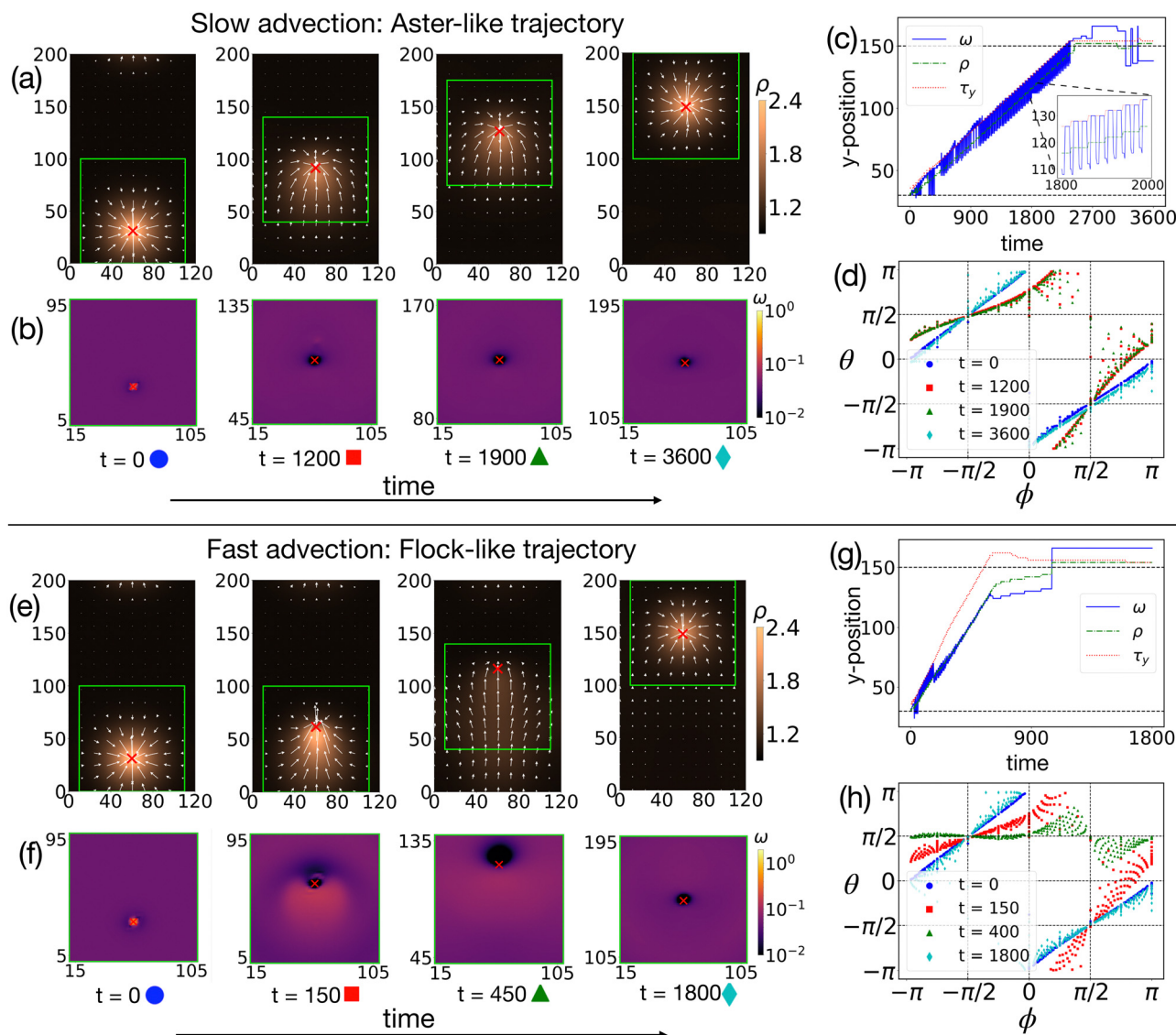
Fig. 3 Prescribing the path and speed of aster advection. The control problem is formulated in two stages: in advection, the aster moves at a mean speed of $\bar{v}$ for t_{adv} time units; in reformation, the aster reacquires its steady-state profile over a timescale t_{reform}. The figure shows two examples. In both cases, the control task is to move the aster by 120 length units in the $\hat{y}$ direction. (a)–(d) Example 1: slower advection, with $\bar{v} = 1/20$, $t_{adv} = 2400$, $t_{reform} = 1200$. (e)–(h) Example 2: faster advection, with $\bar{v} = 1/5$, $t_{adv} = 600$, $t_{reform} = 1200$. (a) and (e) Snapshots of the density (color map) and polarization (arrows) profiles for examples 1 (a) and 2 (e). For both examples, snapshots are shown for the initial state $t = 0$, two intermediate times during the advection phase, and the final point at $t = 3600$ (slow)/$t = 1800$ (fast). (b) and (f) Corresponding snapshots for the activity field (color map). The 'x' symbols in the snapshots in ((a), (b), (e) and (f)) show the position of the aster core. (c) and (g) Tracking the progress of the aster and the control solution. The plot shows the y-components of the position corresponding to the aster core (density maximum, ρ, green curve); activity maximum (ω, blue curve); and the minimum torque (τ_y, red curve). (d) and (h) The polarization direction θ as a function of the azimuthal angle ϕ, measured at a distance $r = 20$ from the aster core, at indicated times. The objective function parameters for both examples are the objective function parameters are $\{A, B, C, D, K, \omega_0\} = \{0.1, 1.0, 2.0, 2.0, 0, 0.05\}$, $\lambda = 0.8$, and the simulation box size is 120×200. Videos corresponding to Examples 1 and 2 are provided in ESI† Movies S2 and S3.

not eliminated by penalizing time variations in activity with nonzero K.[77] The oscillatory behavior is evident in Fig. 3c, which shows the positions of the maxima of ρ and ω and the minimum of the y-component of the torque, τ_y, as a function of time. The maximum in the control solution ω exhibits strong oscillations of 20 length units between the front and rear of the aster (while the activity remains low at the aster core, see Fig. 3b), whereas the density maximum moves at a nearly continuous speed toward the target. The minimum τ_y tracks

polarization toward the $-\hat{y}$ direction and it consistently coincides with the high activity point at the front of the aster. Taken together, these observations show that the control solution pushes the aster from the rear, while exerting torques at the front that maintain aster-like polarization. This is captured in Fig. 3d which shows θ as a function of the azimuthal angle ϕ at two intermediate times during the advection phase, $t = 1200$ and 1900. Finally, during the second (reformation) phase, the aster re-acquires its radially symmetric steady state density and

polarization profile. The dynamical interplay among these forces can be seen in the ESI.†

Since we are specifying the path of the aster, we can investigate how the control solution depends on the chosen advection rate. Fig. 3e–h shows analogous results for a trajectory in which the advection phase is shortened to $t_{adv} = 600$, forcing a higher translation speed $\bar{v} = 1/5$. The higher speed leads to a qualitatively different type of trajectory; the aster unwinds into a flock during the advection phase, and then reforms during the second phase. Here the control solution takes a bean-shaped spatial profile, which initially pulsates periodically to unwind the leading edge of the aster and push the aster toward the target position. At early times (by $t = 150$) the rear of the aster adopts a flock-like state with polarization primarily pointing in the $\hat{y}$-direction; by $t = 450$ most of the aster becomes flock-like. The extent of polarization along $\hat{y}$ is particularly clear from the plot of $\theta(\phi)$ at $t = 450$ (Fig. 3h, green triangles).

The trajectories in Fig. 3 demonstrate that imposing different constraints in the control problem, such as the time duration, can lead to very different activity profiles and intermediate states in the optimal solution. We can qualitatively, but not quantitatively, understand the transition from aster-like to flock-like behaviors to result from higher values of activity ω required to meet the imposed advection speed (due to the shorter time duration). In addition to setting the effective self-propulsion speed, the activity ω controls the effective compressibility of the active fluid, with small values of ω corresponding to negative compressibilities that favor asters and large values corresponding to positive compressibilities that favor polar flocks. These behaviors are evident in the phase diagram of the uncontrolled system (Fig. 1a). For the value of the particle interaction coefficient $\lambda = 0.8$, the uncontrolled system steady-state transitions from asters to 'blobs' to polar flocks at about $\omega = 0.2$ and $\omega = 0.25$. Thus, we might expect the system to at least locally undergo a transition out of the aster state above a threshold advection speed and corresponding local activity. However, due to the significant spatial variations of omega in the control solution, we cannot quantitatively connect the trajectory transition to the phase diagram. In particular, we observe maximum activity values (taken over space and time) of $\omega_{max} = 0.9$ and 1.6 for the slow and fast advection trajectories respectively, meaning that the maximum local activity value is well above the phase transition threshold even for the aster-like trajectory.

B. Changing the direction of propagating stripes

Next, starting at a parameter set for which stripes are stable, we obtain an activity profile to change the stripe propagation direction, with initial direction along $+\hat{x}$ and a target direction diagonally oriented along 45°. Note that we obtain similar results for any target orientation, including reversing the stripe direction by 180°. Fig. 4a and b show the system configurations and corresponding control solutions at several time points. At $t = 0$, the applied activity is strongest at the leading edge of the stripe, and decays over the width of the leading boundary

layer (*i.e.*, the region where the polarization changes from isotropic to uniform). These gradients in activity lead to both melting (reduction of the magnitude of polarization) and turning (reorientation of polarization toward the target direction). At the next two time-points ($t = 100, 200$) the activity has decreased in magnitude, but continues to turn the polarization. By $t = 500$ the activity is nearly uniform in space and approaching its steady-state value of 0.4. However, some curvature remains near the leading edge of the stripe. The stripe has completely reformed by the last time point ($t = 1400$). Notably, the timescale for dissolving and reorienting the stripes at this periodic box size 256 × 256 (ESI,† Movie S4) was about 500 in our dimensionless units, which is 2 orders of magnitude lower than obtaining stripes from a random homogenous initial condition in the absence of control.

While a straightforward route to reorienting a strip would be to melt the stripe to an isotropic domain and then have it reform in the new direction, this is not the optimal solution given by the control theory. Starting with the density equation, eqn (3), we investigate the primary forces influencing density evolution during the stripe reorientation process. For this we choose a subdomain $0 < x \leq 50$, $0 < y \leq 100$ within the simulation box of size 256 × 256. We integrate each of the three terms in eqn (3) over the specified subdomain as a function of time (Fig. 4c): $-\omega\nabla\cdot\tau$, which governs the convection of active particles at convection speed ω; $-\tau\cdot\nabla\omega$, which determines the local density dynamics due to gradients in activity; and $\nabla^2\rho$, which determines the diffusion due to density gradients. We find that, at all times, the dominant contribution arises from self-propulsion, $-\omega\nabla\cdot\tau$; contributions from gradients in activity and density have negligible contributions. Thus, we conclude that activity gradients are not the driving force for the density dynamics, but rather lead to the torques that reorient the polarization field, as described in our analysis in Section IV A. To quantify the effect of active torque in this case, we illustrate in Fig. 4c that as the difference in orientation between the initial state and target state increases, the active torque also increases, and as the system settles into the target orientation, the active torque goes to 0.

This result can be qualitatively understood as follows. A trajectory which proceeds through an isotropic intermediate state would require large magnitudes and gradients of activity to melt the stripe and then reform it in a new direction. Instead, the optimal solution takes advantage of the fact that a stripe arises through a spontaneous breaking of rotational symmetry, and thus requires only small torques (and correspondingly small orientational biases in gradients of activity) to reorient its direction.

C. Remodeling stripe to aster

So far, we have considered cases where the initial and target states are both steady states of the uncontrolled forward dynamics of our system at specified parameters. To demonstrate the power of the control theory, we start in a parameter regime in which propagating stripes are stable, and obtain an activity profile that drives the system into a stationary aster
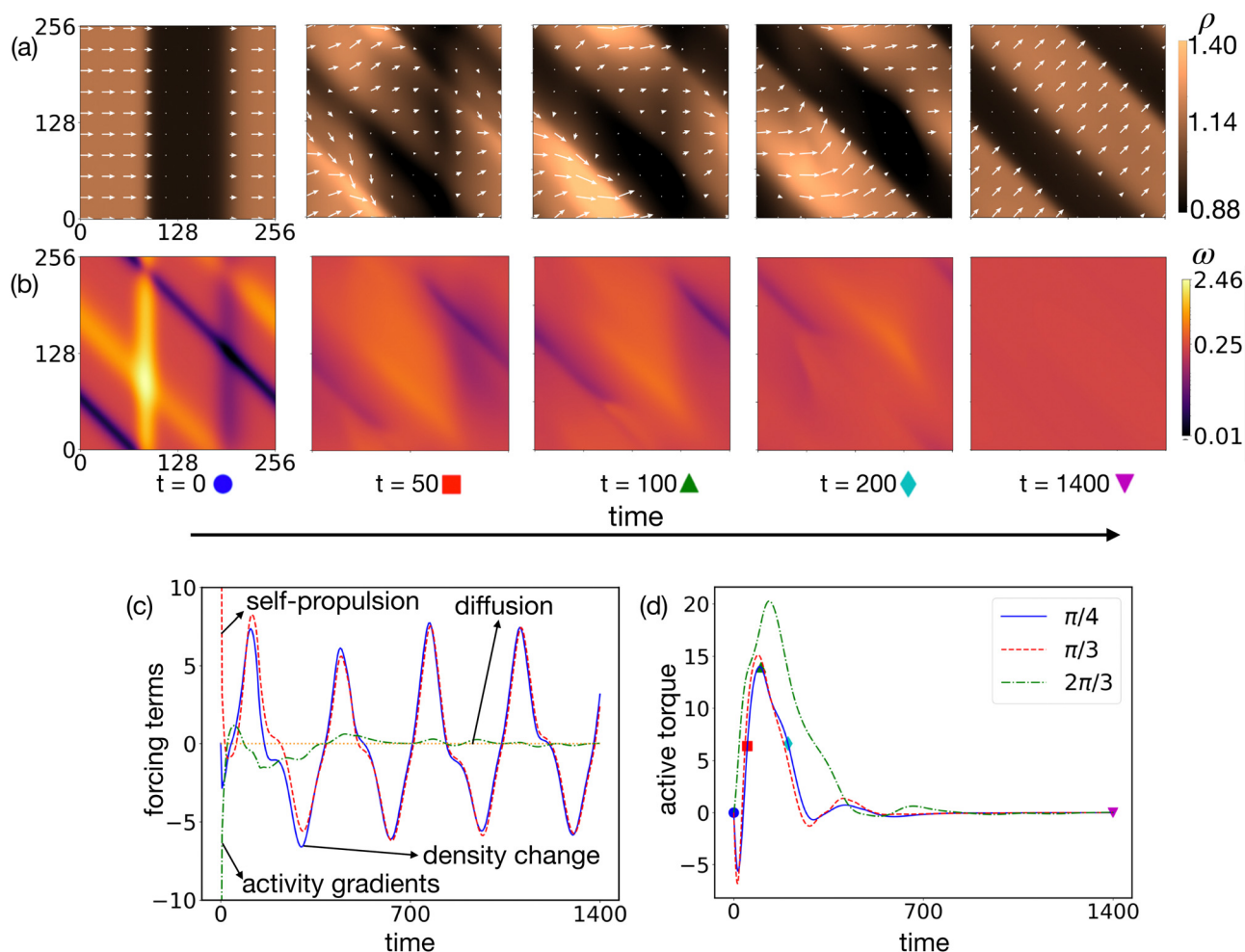
Fig. 4 Changing the propagation direction of stripes. (a) and (b) Snapshots of (a) the density (color map) and polarization (arrows) profiles and (b) the activity field ω (color map). The system is initialized in an unperturbed stripe steady-state traveling in the $+\hat{x}$ direction, with parameters $\{\omega, \lambda\} = \{0.4, 0.0\}$. The control solution begins at $t = 0$ and the system state is shown at indicated times. (c) Contribution of each term of the density dynamics, (3), evaluated by integration across the defined sub-domain: Ω_δ: $0 < x \leq 50$ and $0 < y \leq 100$ (see Section IV B). The terms are: $\int_{\Omega_\delta} \partial t \rho$ (density change), which is driven by $-\omega \boldsymbol{\nabla} \cdot \boldsymbol{\tau}$ (self-propulsion), $-\boldsymbol{\tau} \cdot \boldsymbol{\nabla} \omega$ (density flow due to activity gradients) and $\boldsymbol{\nabla}^2 \rho$ (diffusion due to density gradients). (d) The active torque $\boldsymbol{\nabla}\omega \times \boldsymbol{\tau}$ integrated over the entire domain with time for different target orientations. The objective function parameters are $\{A, B, C, D, K, \omega_0\} = \{0.1, 1.0, 7.0, 7.0, 0, 0.4\}$; $\lambda = 0.0$, and the simulation box size is 256×256. Videos S4 and S6 (ESI†) respectively show this trajectory and an independent run in which the stripe is forced to re-orient by $90°$.

(not a steady state at these parameters). For the initial condition, we run to steady-state under parameters that lead to propagating stripes, $\lambda = 0.6$ and $\omega = 0.4$. To obtain a configuration to specify the target state, we perform an independent simulation in which we obtain a stationary aster steady-state with $\lambda = 0.6$ and $\omega = 0.04$. Fig. 5 shows the trajectory and corresponding control solution. We see that at early times the applied activity is strongest at the top- and bottom-edges of the leading boundary layer of the stripe, which bends the polarization vectors toward the core of the target aster. The magnitude of the activity field decreases quickly in time, but the spatial profile remains similar, thus continuing to steer polarization toward the core, and decreasing the net momentum in the $+\hat{x}$ direction. Due to the coupling between ρ and $\boldsymbol{\tau}$ (see eqn (3)), the resulting gradients and polarization lead to convection of density toward the core. By $t = 1500$, there is a density

maximum at the core and the system has achieved a radially symmetric state, which leads to a balance of propulsion forces and thus a stationary state.

We note that this control problem also differs from the previous one (reorienting stripes) in that the initial and final state have different symmetries. However, the optimal solution still avoids isotropic intermediate states, since these would require significantly larger magnitudes and gradients of activity.

D. Robustness of the optimal control solution to noise and parameter variations

Since models are never completely accurate and noise is inevitable in any experimental system, we investigated the robustness of our control solution to noise and parameter variations. Because our implementation uses deterministic
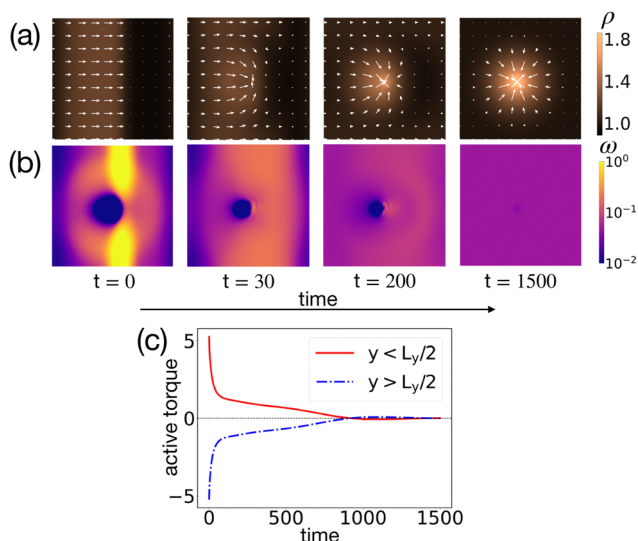
Fig. 5 Remodelling a propagating stripe to a stationary aster. The system is initialized in an unperturbed stripe steady-state traveling in the $+\hat{x}$ direction, with parameters $\{\omega, \lambda\} = \{0.4, 0.6\}$ seeded at $(x_0 = 60, y_0 = 60)$. The target state is obtained from a simulation of an aster steady state with parameters $\{\omega, \lambda\} = \{0.04, 0.6\}$. (a) and (b) Snapshots of (a) the density (color map) and polarization (arrows) profiles and (b) the activity field (color map). The final activity is equal to the activity of the steady state aster, $\omega = 0.04$ everywhere except near the defect core, where it approaches zero. The baseline activity $\omega_0 = 0.4$ was set to the value corresponding to the stripe steady state. (c) The active torque $\nabla\omega \times \tau$ integrated over time for each of the two subdomains $0 < x \leq L_x$, $0 < y \leq L_y/2$ and $L_y/2 < y \leq L_y$. The objective function parameters are $\{A, B, C, D, K, \omega_0\} = \{0.1, 1.0, 5.5, 5.5, 0, 0.4\}$; $\lambda = 0.6$; and the simulation box size is 128×128. A video of this trajectory is in ESI† Movie S5.

PDEs, we tested the effects of noise by perturbing the initial condition for the aster translocation problem presented in Fig. 2. Specifically, we added Gaussian noise with a relative

magnitude ϵ_n to the values of ρ, τ_x, and τ_y at each pixel, and then integrated the dynamics with the control protocol computed in the absence of noise. Fig. 6 shows the performance of the control solution. We plot the deviation from the trajectory integrated with zero noise and $\lambda = 0.8$ (see Fig. 2a):

$$\mathcal{J}_T(t) = \frac{1}{\Omega}\int_\Omega d\mathbf{r}\frac{1}{2}\Big[(\rho(\mathbf{r}, t) - \rho^\star(\mathbf{r}, t))^2 + (\tau(\mathbf{r}, t) - \tau^\star(\mathbf{r}, t))^2\Big],$$

(10)

where $(\rho^\star(\mathbf{r},t), \tau^\star(\mathbf{r},t))$ is the trajectory in Fig. 2a and the error is normalized by the spatial extent Ω. The inset shows the deviation of the final state from the target $\mathcal{J}_T(t_F)$, as a function of ϵ_n. We see that noise has a relatively small effect on the performance up to a magnitude of about $\epsilon_n = 20\%$, after which deviations in the objective function rise dramatically. However, even with $\epsilon_n = 35\%$ and a relatively large value of $\mathcal{J} \approx 0.021$ at t_F, the final state is remarkably close to the target in all qualitative aspects (see Fig. 6c), with a well-formed aster close to the target position. Thus, we conclude that the optimal control solution is robust to noise, at least in the initial condition.

To investigate the effect of model parameter errors on the optimal control solution, we performed trials for the aster advection problem shown in Fig. 2 with varying λ. That is, we used the same initial condition and the optimal protocol computed with $\lambda = 0.8$ (*i.e.* the activity sequence shown in Fig. 2b), but we integrated the equations of motion with different values of λ. As shown in Fig. 7, we see small errors for variations in λ smaller than 10%, beyond which the errors rise significantly. However, similar to the noise results, we observe well-formed asters even for cases with large variations, although their final positions deviate from the target state (Fig. 7c).
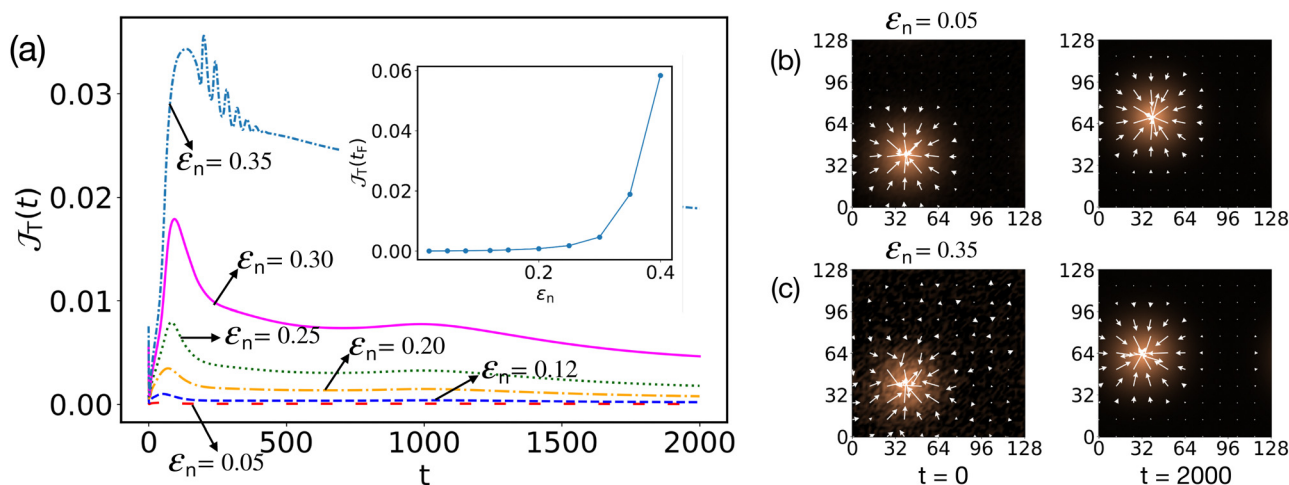

Fig. 6 Robustness of the control solution to adding noise to the initial condition. (a) Deviation as a function of time between the trajectories integrated computed with and without noise ($\mathcal{J}_T$, eqn (10)). We added Gaussian noise to the initial condition with indicated magnitude ϵ_n, and integrated the dynamics using the control protocol computed in the absence of noise ($\epsilon_n = 0$) that is shown in Fig. 2. The inset shows the deviation of the final state $\mathcal{J}_T(t_F)$ as a function of noise magnitude ϵ_n. (b) and (c) The initial and final states for (b) small ($\epsilon_n = 0.05$) and (c) large ($\epsilon_n = 0.35$) noise. We see robust aster structures even when the error is large in the end state for 35% noise. Parameter values are as in Fig. 2.
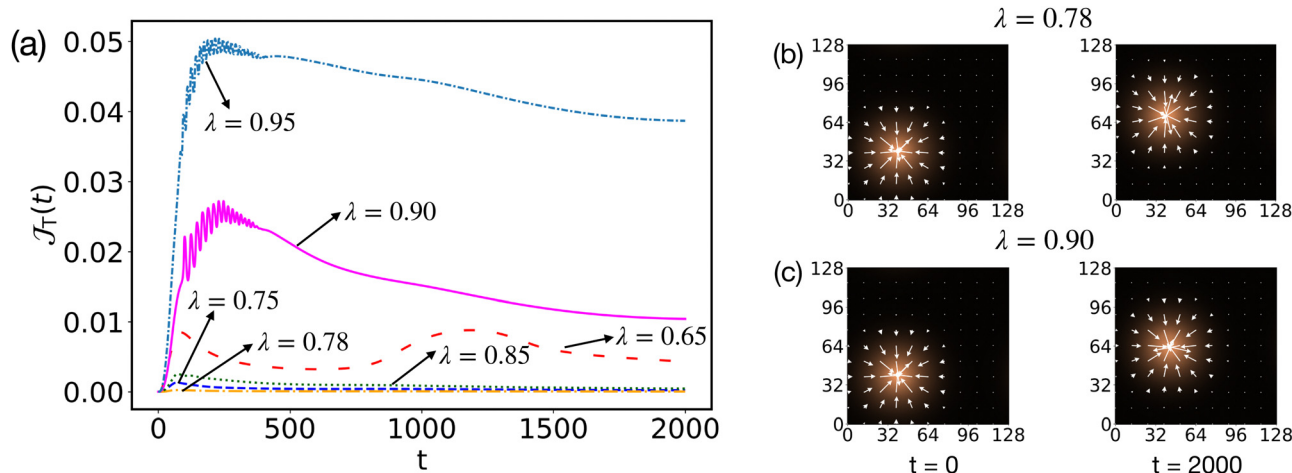
Fig. 7 Robustness of the control solution to variations in the model parameter λ. (a) The deviation $\mathcal{J}_T$ between the trajectory integrated with the optimal control protocol from Fig. 2b but with the indicated value of λ, compared to the one with $\lambda = 0.8$ shown in Fig. 2b. (b) and (c) Snapshots showing the initial and final states for (b) relatively small ($\lambda = 0.78$) and (c) large ($\lambda = 0.9$) parameter variations. We observe well-formed aster structures even though the error is relatively large at the end state for $\lambda = 0.9$, although the aster position deviates from the target. Parameter values are as in Fig. 2.

V. Discussion and conclusions

We demonstrate an optimal control theory framework that can prescribe activity patterns to guide an active material into desired emergent behaviors, focusing on an active polar fluid as a model system. The capabilities include programmed switching among dynamical attractors with very different dynamics and distinct broken symmetry patterns, and reprogramming the dynamics of existing attractor states. As an example of the former, we identify a spatiotemporal activity pattern that converts a propagating stripes state into a stationary aster. As an example of the latter, we show that a stationary aster can be programmed to self-advect to a new target configuration, either *via* an arbitrary trajectory or along a prescribed path. Similarly, propagating stripes can be forced to reorient in arbitrary directions. Depending on the choice of terms and weights in the objective function, the spatiotemporal variations of the control inputs can be regulated to limit experimental cost or ensure smooth trajectories.

Further, we show that the optimal control solutions are robust to noise. In particular, perturbing the initial condition by up to 20% leads to minimal quantitative deviations from the target behavior, and the solution remains qualitatively accurate for significantly larger perturbations. Also, we note that additional strategies can be employed for experimental systems where larger noise sources or systematic errors are unavoidable. This includes integrating closed-loop control components. For example, one can observe the current state of the system at regular intervals along a trajectory, and recompute the optimal control solution using the current state as the initial condition. Alternatively, one can add linear feedback terms that analyze deviations from the pre-computed optimal control trajectory.[78]

In addition to directly applying the computed activity protocols, examination of their forms provides both fundamental and practical insights into controlling active materials. In particular,

we show how the spatial gradients in the applied activity field lead to localized torques which rotate polarization directions, leading to the programmed reformulation of the pattern of interest (*e.g.* aster or stripe). Unsurprisingly, the form of the trajectory is different depending on the task being encoded for – changing the broken symmetry state of the system (*e.g.* stripe-to-aster, Fig. 5) requires very different spatial arrangements of active torques then advection (Fig. 2 and 3) or reorientation (Fig. 4). Notably however, the applied activity field and corresponding trajectory also depend strongly on the time allowed for the transformation. In the example of advecting the aster over a distance many times its size (Fig. 3), the aster mostly retains its form throughout the course of the trajectory when moving at moderate speed, but when forced to complete the journey $4\times$ faster, the applied activity field reshapes the aster into a localized flock or swarm, which reformulates into an aster upon reaching the target position.

The states we seek to control are realizable in experiments. Propagating concentration waves of aligned self-propelled particles have been observed in dense actin motility assays[79–82] and in self-chemotactic bacterial systems.[83–91] Asters are ubiquitous in cell biology in processes such as the formation of the mitotic spindle, oogenesis, and plant cell cytokinesis.[92–99] They can be reliably obtained in *in vitro* suspensions of cytoskeletal filaments and motor proteins.[6,46,95,100–110] In such systems, activity can be controlled in space and time by constructing active materials with optogenetic molecular motors. For example, the closely related microtubule-based active nematic system has been modified to contain light-activated kinesins clusters, so that the activity is proportional to the local light intensity.[43–46] The researchers then used a digital light projector to shine programmed spatiotemporal sequences of light on the sample.[43–46] Our optimal control protocol can be used to determine the spatiotemporal light sequence that will drive such a system into a desired state. Due to inevitable accuracies

in hydrodynamic descriptions of active matter systems and experimental noise, it is important that we found our optimal control solutions to be robust against noise and parameter inaccuracies (Fig. 6 and 7). Further, optimal control solutions can be corrected by periodically observing the state of the system and applying feedback control. For example, feedback can be implemented by adding linear restoring forces that drive the system toward the computed trajectory, or by recomputing the optimal control solution based on the current state of the system.

The optimal control framework presented here is highly generalizable, and can be readily applied to any system provided there is a means to externally actuate the system and there is a reasonably accurate continuum model. Importantly, the control variable need not be limited to the activity field, since the objective function can be extended to include any property of the material that can be actuated. With the recent success of automated PDE learning tools in discovering continuum models for active systems (e.g. ref. 111–113), applications need not be limited to systems with accurate models already available. Furthermore, since model discovery tools work better when provided with a variety of data, including from non-steady-state observations, we anticipate that combining model discovery tools with optimal control could be a powerful approach to both discover more accurate models and enhance the reliability of the control solutions.

Data availability

The code and data associated with this work are provided in: **https://github.com/ghoshsap/optimal-control-activepolarfluid/tree/main**.

Conflicts of interest

There are no conflicts to declare.

Acknowledgements

References

1 K.-A. Liu and I. Lin, *Phys. Rev. E: Stat., Nonlinear, Soft Matter Phys.*, 2012, **86**, 011924.
2 A. Czirók and T. Vicsek, *Phys. A*, 2000, **281**, 17–29.
3 C. Pierce, H. Wijesinghe, E. Mumper, B. Lower, S. Lower and R. Sooryakumar, *Phys. Rev. Lett.*, 2018, **121**, 188001.
4 D. Needleman and Z. Dogic, *Nat. Rev. Mater.*, 2017, **2**, 1–14.
5 G. Sarfati, A. Maitra, R. Voituriez, J.-C. Galas and A. Estevez-Torres, *Soft Matter*, 2022, **18**, 3793–3800.
6 F. Ndlec, T. Surrey, A. C. Maggs and S. Leibler, *Nature*, 1997, **389**, 305–308.
7 T. Surrey, F. Nédélec, S. Leibler and E. Karsenti, *Science*, 2001, **292**, 1167–1171.
8 M. L. Gardel, K. E. Kasza, C. P. Brangwynne, J. Liu and D. A. Weitz, *Methods Cell Biol.*, 2008, **89**, 487–519.
9 M. L. Gardel, I. C. Schneider, Y. Aratyn-Schaus and C. M. Waterman, *Annu. Rev. Cell Dev. Biol.*, 2010, **26**, 315–333.
10 M. Dogterom and G. H. Koenderink, *Nat. Rev. Mol. Cell Biol.*, 2019, **20**, 38–54.
11 M. Soarese Silva, M. Depken, B. Stuhrmann, M. Korsten, F. C. MacKintosh and G. H. Koenderink, *Proc. Natl. Acad. Sci. U. S. A.*, 2011, **108**, 9408–9413.
12 C. G. Wagner, M. M. Norton, J. S. Park and P. Grover, *Phys. Rev. Lett.*, 2022, **128**, 028003.
13 W. Wang, W. Duan, S. Ahmed, A. Sen and T. E. Mallouk, *Acc. Chem. Res.*, 2015, **48**, 1938–1946.
14 J. R. Gomez-Solano, S. Samin, C. Lozano, P. RuedasBatuecas, R. van Roij and C. Bechinger, *Sci. Rep.*, 2017, 7, 14891.
15 O. Hallatschek, S. S. Datta, K. Drescher, J. Dunkel, J. Elgeti, B. Waclaw and N. S. Wingreen, *Nat. Rev. Phys.*, 2023, 1–13.
16 S. Liu, S. Shankar, M. C. Marchetti and Y. Wu, *Nature*, 2021, **590**, 80–84.
17 A. E. Hamby, D. K. Vig, S. Safonova and C. W. Wolgemuth, *Sci. Adv.*, 2018, 4, eaau0125.
18 B. Ni, R. Colin, H. Link, R. G. Endres and V. Sourjik, *Proc. Natl. Acad. Sci. U. S. A.*, 2020, **117**, 595–601.
19 E. Lauga and T. R. Powers, *Rep. Prog. Phys.*, 2009, **72**, 096601.
20 D. Gonzalez-Rodriguez, K. Guevorkian, S. Douezan and F. Brochard-Wyart, *Science*, 2012, **338**, 910–917.
21 S. Henkes, K. Kostanjevec, J. M. Collinson, R. Sknepnek and E. Bertin, *Nat. Commun.*, 2020, **11**, 1405.
22 E. Fodor and M. C. Marchetti, *Phys. A*, 2018, **504**, 106–120.
23 J. W. Nichol and A. Khademhosseini, *Soft Matter*, 2009, **5**, 1312–1319.
24 G. Zhang, R. Mueller, A. Doostmohammadi and J. M. Yeomans, *J. R. Soc., Interface*, 2020, **17**, 20200312.
25 A. Doostmohammadi, S. P. Thampi and J. M. Yeomans, *Phys. Rev. Lett.*, 2016, **117**, 048102.
26 T. B. Saw, A. Doostmohammadi, V. Nier, L. Kocgozlu, S. Thampi, Y. Toyama, P. Marcq, C. T. Lim, J. M. Yeomans and B. Ladoux, *Nature*, 2017, **544**, 212–216.
27 X. Trepat, M. R. Wasserman, T. E. Angelini, E. Millet, D. A. Weitz, J. P. Butler and J. J. Fredberg, *Nat. Phys.*, 2009, **5**, 426–430.

28 X. Trepat and E. Sahai, *Nat. Phys.*, 2018, **14**, 671–682.

29 G. Duclos, S. Garcia, H. Yevick and P. Silberzan, *Soft Matter*, 2014, **10**, 2346–2353.

30 C. Blanch-Mercader, V. Yashunsky, S. Garcia, G. Duclos, L. Giomi and P. Silberzan, *Phys. Rev. Lett.*, 2018, **120**, 208101.

31 S. Garcia, E. Hannezo, J. Elgeti, J.-F. Joanny, P. Silberzan and N. S. Gov, *Proc. Natl. Acad. Sci. U. S. A.*, 2015, **112**, 15314–15319.

32 M. Ghibaudo, A. Saez, L. Trichet, A. Xayaphoummine, J. Browaeys, P. Silberzan, A. Buguin and B. Ladoux, *Soft Matter*, 2008, **4**, 1836–1843.

33 T. Vicsek and A. Zafeiris, *Phys. Rep.*, 2012, **517**, 71–140.

34 H. Chaté, *Annu. Rev. Condens. Matter Phys.*, 2020, **11**, 189–212.

35 A. Doostmohammadi, J. Ignés-Mullol, J. M. Yeomans and F. Sagués, *Nat. Commun.*, 2018, **9**, 1–13.

36 C. Bechinger, R. Di Leonardo, H. Löwen, C. Reichhardt, G. Volpe and G. Volpe, *Rev. Mod. Phys.*, 2016, **88**, 045006.

37 G. Gompper, R. G. Winkler, T. Speck, A. Solon, C. Nardini, F. Peruani, H. Löwen, R. Golestanian, U. B. Kaupp and L. Alvarez, *et al.*, *J. Phys.: Condens. Matter*, 2020, **32**, 193001.

38 M. C. Marchetti, J.-F. Joanny, S. Ramaswamy, T. B. Liverpool, J. Prost, M. Rao and R. A. Simha, *Rev. Mod. Phys.*, 2013, **85**, 1143.

39 A. Aubret, M. Youssef, S. Sacanna and J. Palacci, *Nat. Phys.*, 2018, **14**, 1114–1118.

40 J. Palacci, S. Sacanna, A. P. Steinberg, D. J. Pine and P. M. Chaikin, *Science*, 2013, **339**, 936–940.

41 J. Arlt, V. A. Martinez, A. Dawson, T. Pilizota and W. C. Poon, *Nat. Commun.*, 2018, **9**, 768.

42 G. Frangipane, D. Dell'Arciprete, S. Petracchini, C. Maggi, F. Saglimbeni, S. Bianchi, G. Vizsnyiczai, M. L. Bernardini and R. Di Leonardo, *eLife*, 2018, **7**, e36608.

43 L. M. Lemma, M. Varghese, T. D. Ross, M. Thomson, A. Baskaran and Z. Dogic, *PNAS Nexus*, 2023, **2**, pgad130.

44 Z. Zarei, J. Berezney, A. Hensley, L. Lemma, N. Senbil, Z. Dogic and S. Fraden, *Soft Matter*, 2023, **19**, 6691–6699.

45 R. Zhang, S. A. Redford, P. V. Ruijgrok, N. Kumar, A. Mozaffari, S. Zemsky, A. R. Dinner, V. Vitelli, Z. Bryant and M. L. Gardel, *et al.*, *Nat. Mater.*, 2021, **20**, 875–882.

46 T. D. Ross, H. J. Lee, Z. Qu, R. A. Banks, R. Phillips and M. Thomson, *Nature*, 2019, **572**, 224–229.

47 S. Shankar, L. V. Scharrer, M. J. Bowick and M. C. Marchetti, *Proc. Natl. Acad. Sci. U. S. A.*, 2024, **121**, e2400933121.

48 M. Nasiri, H. Löwen and B. Liebchen, *Europhys. Lett.*, 2023, **142**, 17001.

49 M. Knežević, T. Welker and H. Stark, *Sci. Rep.*, 2022, **12**, 19437.

50 S. L. Brunton and J. N. Kutz, *Data-driven science and engineering: Machine learning, dynamical systems, and control*, Cambridge University Press, 2022.

51 G. E. Dullerud and F. Paganini, *A course in robust control theory: a convex approach*, Springer Science & Business Media, 2013, vol. 36.

52 C. Villani, *et al.*, *Optimal transport: old and new*, Springer, 2009, vol. 338.

53 M. M. Norton, P. Grover, M. F. Hagan and S. Fraden, *Phys. Rev. Lett.*, 2020, **125**, 178005.

54 C. Sinigaglia, F. Braghin and M. Serra, *Phys. Rev. Lett.*, 2024, **132**, 218302.

55 J. Toner and Y. Tu, *Phys. Rev. Lett.*, 1995, **75**, 4326.

56 J. Toner and Y. Tu, *Phys. Rev. E: Stat. Phys., Plasmas, Fluids, Relat. Interdiscip. Top.*, 1998, **58**, 4828.

57 H. Y. Lee and M. Kardar, *Phys. Rev. E: Stat., Nonlinear, Soft Matter Phys.*, 2001, **64**, 056113.

58 K. Husain and M. Rao, *Phys. Rev. Lett.*, 2017, **118**, 078104.

59 D. Geyer, A. Morin and D. Bartolo, *Nat. Mater.*, 2018, **17**, 789–793.

60 V. M. Worlitzer, G. Ariel, A. Be'er, H. Stark, M. Bär and S. Heidenreich, *New J. Phys.*, 2021, **23**, 033012.

61 S. Mishra, A. Baskaran and M. C. Marchetti, *Phys. Rev. E: Stat., Nonlinear, Soft Matter Phys.*, 2010, **81**, 061916.

62 A. Gopinath, M. F. Hagan, M. C. Marchetti and A. Baskaran, *Phys. Rev. E: Stat., Nonlinear, Soft Matter Phys.*, 2012, **85**, 061903.

63 J.-B. Caussin, A. Solon, A. Peshkov, H. Chaté, T. Dauxois, J. Tailleur, V. Vitelli and D. Bartolo, *Phys. Rev. Lett.*, 2014, **112**, 148102.

64 H. Reinken, S. H. L. Klapp, M. Bär and S. Heidenreich, *Phys. Rev. E*, 2018, **97**, 022613.

65 W. Ngamsaad and S. Suantai, *Phys. Rev. E*, 2018, **98**, 062618.

66 E. Bertin, M. Droz and G. Grégoire, *Phys. Rev. E: Stat., Nonlinear, Soft Matter Phys.*, 2006, **74**, 022101.

67 A. Peshkov, I. S. Aranson, E. Bertin, H. Chaté and F. Ginelli, *Phys. Rev. Lett.*, 2012, **109**, 268701.

68 A. Baskaran and M. C. Marchetti, *Phys. Rev. Lett.*, 2008, **101**, 268101.

69 P. Srivastava, R. Shlomovitz, N. S. Gov and M. Rao, *Phys. Rev. Lett.*, 2013, **110**, 168104.

70 G. I. Menon, *Rheology of complex Fluids*, 2010, pp. 193–218.

71 A. P. Solon and J. Tailleur, *Phys. Rev. Lett.*, 2013, **111**, 078101.

72 D. E. Kirk, *Optimal control theory: an introduction*, Courier Corporation, 2004.

73 S. Lenhart and J. T. Workman, *Optimal control applied to biological models*, Chapman and Hall/CRC, 2007.

74 R. Kerswell, C. C. Pringle and A. Willis, *Rep. Prog. Phys.*, 2014, **77**, 085901.

75 A. Borzí and V. Schulz, *Computational optimization of systems governed by partial differential equations*, SIAM, 2011.

76 T. Dupont, J. Hoffman, C. Johnson, R. C. Kirby, M. G. Larson, A. Logg and L. R. Scott, *The fenics project, Chalmers Finite Element Centre*, Chalmers University of Technology, 2003.

77 At least up to $K = 1$, larger values led to convergence problems. We expect that interpolating the target state would lead to a smoother solution profile.

78 J. Bechhoefer, *Control Theory for Physicists*, Cambridge University Press, 2021.

79 V. Schaller, C. Weber, C. Semmrich, E. Frey and A. R. Bausch, *Nature*, 2010, **467**, 73–77.

80 L. Huber, R. Suzuki, T. Krüger, E. Frey and A. Bausch, *Science*, 2018, **361**, 255–258.

81 A. Sciortino and A. R. Bausch, *Proc. Natl. Acad. Sci. U. S. A.*, 2021, **118**, e2017047118.

82 R. Suzuki and A. R. Bausch, *Nat. Commun.*, 2017, **8**, 41.

83 J. Saragosti, V. Calvez, N. Bournaveas, B. Perthame, A. Buguin and P. Silberzan, *Proc. Natl. Acad. Sci. U. S. A.*, 2011, **108**, 16235–16240.

84 O. Pohl and H. Stark, *Phys. Rev. Lett.*, 2014, **112**, 238303.

85 T. Bhattacharjee, D. B. Amchin, R. Alert, J. A. Ott and S. S. Datta, *eLife*, 2022, **11**, e71226.

86 R. Alert, A. Martínez-Calvo and S. S. Datta, *Phys. Rev. Lett.*, 2022, **128**, 148101.

87 A. V. Narla, J. Cremer and T. Hwa, *Proc. Natl. Acad. Sci. U. S. A.*, 2021, **118**, e2105138118.

88 J. Cremer, T. Honda, Y. Tang, J. Wong-Ng, M. Vergassola and T. Hwa, *Nature*, 2019, **575**, 658–663.

89 T. Bhattacharjee, D. B. Amchin, J. A. Ott, F. Kratz and S. S. Datta, *Biophys. J.*, 2021, **120**, 3483–3497.

90 M. P. Brenner, L. S. Levitov and E. O. Budrene, *Biophys. J.*, 1998, **74**, 1677–1693.

91 C. Fei, S. Mao, J. Yan, R. Alert, H. A. Stone, B. L. Bassler, N. S. Wingreen and A. Košmrlj, *Proc. Natl. Acad. Sci. U. S. A.*, 2020, **117**, 7622–7632.

92 T. U. Mayer, T. M. Kapoor, S. J. Haggarty, R. W. King, S. L. Schreiber and T. J. Mitchison, *Science*, 1999, **286**, 971–974.

93 S. C. Schaffner and J. V. José, *Proc. Natl. Acad. Sci. U. S. A.*, 2006, **103**, 11166–11171.

94 R. Loughlin, R. Heald and F. Nédélec, *J. Cell Biol.*, 2010, **191**, 1239–1249.

95 M. Shirasu-Hiza, Z. E. Perlman, T. Wittmann, E. Karsenti and T. J. Mitchison, *Curr. Biol.*, 2004, **14**, 1941–1945.

96 S. R. Heidemann and M. W. Kirschner, *J. Cell Biol.*, 1975, **67**, 105–117.

97 S. R. Heidemann and M. W. Kirschner, *J. Exp. Zool.*, 1978, **204**, 431–443.

98 A.-C. Schmit, M. Vantard, J. De Mey and A.-M. Lambert, *Plant Cell Rep.*, 1983, **2**, 285–288.

99 F. Kumagai and S. Hasezawa, *Plant Biol.*, 2001, **3**, 4–16.

100 B. Najma, W.-S. Wei, A. Baskaran, P. J. Foster and G. Duclos, *Proc. Natl. Acad. Sci. U. S. A.*, 2024, **121**, e2300174121.

101 V. Wollrab, J. M. Belmonte, L. Baldauf, M. Leptin, F. Nédéléc and G. H. Koenderink, *J. Cell Sci.*, 2019, **132**, jcs219717.

102 P. J. Foster, S. Fürthauer, M. J. Shelley and D. J. Needleman, *eLife*, 2015, **4**, e10837.

103 A. Colin, P. Singaravelu, M. Théry, L. Blanchoin and Z. Gueroui, *Curr. Biol.*, 2018, **28**, 2647–2656.

104 W. Luo, C.-H. Yu, Z. Z. Lieu, J. Allard, A. Mogilner, M. P. Sheetz and A. D. Bershadsky, *J. Cell Biol.*, 2013, **202**, 1057–1073.

105 S. Stam, S. L. Freedman, S. Banerjee, K. L. Weirich, A. R. Dinner and M. L. Gardel, *Proc. Natl. Acad. Sci. U. S. A.*, 2017, **114**, E10037–E10045.

106 J. Berezney, B. L. Goode, S. Fraden and Z. Dogic, *Proc. Natl. Acad. Sci. U. S. A.*, 2022, **119**, e2115895119.

107 T. Thoresen, M. Lenz and M. L. Gardel, *Biophys. J.*, 2011, **100**, 2698–2705.

108 D. V. Köster, K. Husain, E. Iljazi, A. Bhat, P. Bieling, R. D. Mullins, M. Rao and S. Mayor, *Proc. Natl. Acad. Sci. U. S. A.*, 2016, **113**, E1645–E1654.

109 M. Glaser, J. Schnauß, T. Tschirner, B. S. Schmidt, M. Moebius-Winkler, J. A. Käs and D. M. Smith, *New J. Phys.*, 2016, **18**, 055001.

110 F. Nédélec, T. Surrey and E. Karsenti, *Curr. Opin. Cell Biol.*, 2003, **15**, 118–124.

111 C. Joshi, S. Ray, L. M. Lemma, M. Varghese, G. Sharp, Z. Dogic, A. Baskaran and M. F. Hagan, *Phys. Rev. Lett.*, 2022, **129**, 258001.

112 R. Supekar, B. Song, A. Hastewell, G. P. Choi, A. Mietke and J. Dunkel, *Proc. Natl. Acad. Sci. U. S. A.*, 2023, **120**, e2206994120.

113 M. Golden, R. O. Grigoriev, J. Nambisan and A. Fernandez-Nieves, *Sci. Adv.*, 2023, **9**, eabq6120.